Comparative study of simultaneous algebraic and filtered backprojection reconstruction methods in digital tomosynthesis for nondestructive testing

Dae Cheon Kim[a], Hanbean Youn[a], Seung Ho Kim[a], Ho Kyung Kim[a,b*]
[a]*School of Mechanical Engineering, Pusan National University, Busan, South Korea*
[b]*Center for Advanced Medical Engineering Research, Pusan National University, Busan, South Korea*
[*]*Corresponding author: hokyung@pusan.ac.kr*

1. Introduction

Several image reconstruction algorithms, such as filtered back projection (FBP), simultaneous algebraic reconstruction technique (SART), and compressed sensing (CS), are available for image reconstruction. These algorithms have their own merits and demerits, in terms of image quality and reconstruction speed. For the industrial applications, such as multi-layer printed circuit board (PCB) inspection, the automated inspection systems require real time imaging and high spatial resolution.

In this study, we quantitatively evaluate the performance of FBP and SART for planar computed tomography (pCT) systems. The performance includes the contrast, and depth resolution. These benefits will be normalized by costs, such as tube loading and speed.

2. Materials and Methods

2.1 Image reconstruction algorithms

The image reconstruction algorithms investigated in this study are FBP and SART. The FBP algorithm is the most typical image reconstruction algorithm in commercial CT product. Since it can calculate slice images analytically, it can provide accurate and fast results. However, there have been reported that several Fourier domain artifacts during the filtering process can occur. In contrary, the SART algorithm calculates the slice images iteratively by solving the algebraic equation. Therefore, SART algorithm can avoid the Fourier domain artifacts. However, the computational complexity originated from iteration is always in issue.

2.2 Filtered Backprojection

The most frequently used image reconstruction algorithm in digital tomosynthesis systems is the Feldkamp (FDK) type algorithm. The FDK approximates the backprojection procedure of cone beam geometry to parallel beam geometry. The FDK algorithm can be represented by following equation [1].

$$f(r)=\oint d\phi \frac{L^2}{(\lambda - r\cdot(n_\zeta \times n_\eta))^2}[\tilde{p}_\phi(\zeta,\eta) * h(\zeta)], \qquad (1)$$

where L is the distance from source to detector, λ is the distance from source to rotation center, and $f(r)$ is an object function in spatial coordinate. $\tilde{p}_\phi(\zeta,\eta)$ (ζ and η represent the orthogonal coordinates in the detector plane) means the projection image multiplied by weighting factor:

$$\tilde{p}_\phi(\zeta,\eta)=\frac{L}{\sqrt{L^2+\zeta^2+\eta^2}}\,p_\phi(\zeta,\eta)\,. \qquad (2)$$

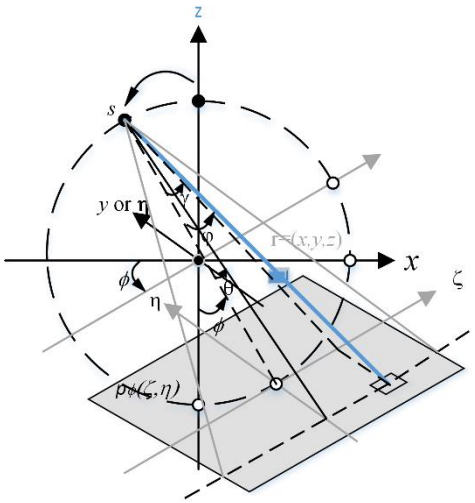

Fig. 1. A sketch describing image reconstruction in cone beam geometry. To reconstruct voxel value at $r=(x,y,z)$, the contribution of projection value at (ζ,η) in the planar detector obtained at the projection angle ϕ is illustrated (see the thick line in the figure). The projection signal is back projected along the line, which is contained in the tilted fan beam [5].

The weighting function defined in equation (1) makes approximately cone beam to parallel beam geometry. $h(\zeta)$ in equation (1) refers to the filter function. The integral operation means the backprojection [5].

In cone beam computed tomography (CBCT) image reconstruction, the calculation of the backprojection indicates the existence of a transfer function that is inversely proportional to frequency. Therefore, an inverse transfer function is needed to compensate the loss. This inverse function is the filter function h. This filter function can be described by the following equation in the spatial frequency domain (u,v).

$$H_{RA}(u,v) = \phi_{scan}\sqrt{u^2+v^2}\ . \tag{3}$$

The ramp filter compensates the low frequency data. However, it amplifies noise in high frequency data. To minimize high frequency noise, we use Hann window function as apodization filter, which is given by

$$H_{SA}(u) = \frac{1}{2}\left[1+\cos(\frac{\pi u}{k_{SA}})\right], \tag{4}$$

where the parameter k_{SA} is window bandwidth, and is represented by multiplies of the Nyquist frequency. This filter is called "spectral apodizing" in Lauritsch and Härer [3, 5].

In digital tomosynthesis (DTS), it requires an additional filter. The DTS obtains data in limited angular ranges. Therefore, deficiencies of data occur along *w*-direction, which is perpendicular to detector plane (*u*, *v*). This causes blur artifact. In order to reduce this artifact, we use the Hann window, which is the same filter as spectral apodizing filter, then we can have:

$$H_{ST}(w) = \frac{1}{2}\left[1+\cos(\frac{\pi u}{k_{ST}})\right], \tag{5}$$

where the parameter k_{ST} represents the bandwidth of window. This is called "slice thickness" filter [3]. We can figure out filter $h(\zeta)$ in equation (1) by combining equations (3), (4), and (5).

2.3 Simultaneous Algebraic Reconstruction Technique

We first introduce the algebraic reconstruction technique (ART). The method of ART in CT is based on line integrals of discrete ray-sum [2]. The ART is an iterative way to figure out following equation:

$$f^{(i)} = f^{(i-1)} + \frac{(p_i - q_i)}{\sum_{k=1}^{N} w_{ik}^2} w_{ij}\ . \tag{6}$$

The limitation of ART is the computational complexity, which is originated from iterative operations in ray by ray. To overcome this issue, the SART algorithm was introduced. The SART improves computational issue of the ART by modifying the updating procedure. Unlike the ART, the SART updates in projection by projection at each iteration [2].

In equation (7), the coefficient a_{ij} is the net influence of the linear transformation, g_j represents the coefficient of expansion which form a finite set of the image *f* [2].

$$g_j^{(k+1)} = g_j^{(k)} + \frac{\sum_i \left[a_{ij} \frac{p_i \vec{a}_i^{\,T} \vec{g}^{(k)}}{\sum_{j=1}^{N} a_{ij}} \right]}{\sum_i a_{ij}}, \tag{7}$$

2.4 Comparison metric

The important image performances of the DTS systems are contrast and depth resolution. To compare these characteristics between the FBP and the SART, we used the quantitative metrics such as signal difference-to-noise ratio (SDNR) and artificial-spread function (ASF). The SDNR characterizes the contrast in the slice images. The SDNR is represented by the following equation:

$$\mathrm{SDNR} = \frac{S_L - S_B}{\sigma_B}, \tag{8}$$

where S_L is signal in the lesion, S_B is signal in the background, and σ_B is noise in the background.

One more important consideration of DTS system is the depth resolution, which is degraded by depth-directional blur artifact caused by the limited angular range of the system. The ASF, which evaluates the depth resolution of DTS systems, was first introduced by Wu *et al* [4]. It is defined by the ratio of pixel intensity between focal plane and the other planes. Therefore, we can have the ASF as [4].

$$\mathrm{ASF} = \frac{S_L(z) - S_B(z)}{S_L(z_0) - S_B(z_0)} \tag{9}$$

where z_0 and z denote the depth of focal plane and the other plane, respectively. Unfortunately, the ASF gives the trend of the blur artifact. Instead, we use half-width at half-maximum (HWHM) of the ASF as a single-valued metric [5].

Finally, we define the figure of merit including the performance of contrast, depth resolution and the system parameters. In this study, we normalize the HWHM with the thickness of phantom, and this parameter defined as Γ. Higher SDNR value means higher signal-to-noise ratio (SNR) in tomosynthesis, and lower value of ASF represents higher vertical direction image quality. Additionally, image reconstruction speed τ increases when total calculation time is increasing. Then, we can have the FOM as [5].

$$\mathrm{FOM} = \frac{\mathrm{SDNR}}{\Gamma \times \tau} \tag{10}$$

2.5 Quantitative phantom

We build the lab-made quantitative phantom to measure the SDNR and ASF simultaneously as shown in Fig. 2. The phantom contains 1-mm-thick aluminum disk inside the 30-mm-diameter PMMA cylinder. At the center slice, we can calculate low contrast SDNR at the nylon region and PMMA region. And the ASF can be also calculated by the same regions at the different depth position.

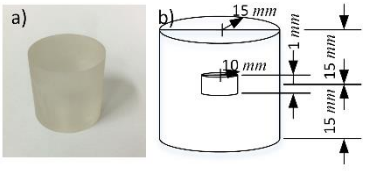

Fig. 2. Cylinder phantom to evaluate SDNR, and ASF. (a) A photograph of the cylinder phantom. (b) Dimensions of the phantom.

3. PRELIMINARY RESULT

Fig. 3 shows the reconstructed slice images of quantitative phantom depicted in fig. 2 by using the FBP algorithm. The projection images are taken from angular range of 60°. The slices are selected at the focal plane (a), -1.7 mm (b), 1.7 mm, and 2.4 mm apart from the focal plane, respectively. Fig. 4 shows the slice images taken from the angular range of 120°. All the imaging parameters except angular range was determined along with 60° case.

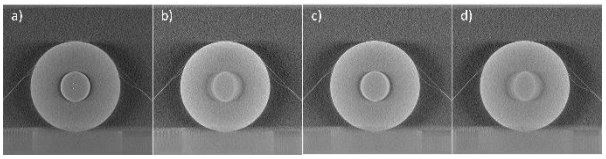

Fig. 3. Result from angular range 60°. (a) z_0, (b) $z=-1.7mm$, (c) $z=1.7\text{mm}$ (d) $z=3.4\text{mm}$ from z_0.

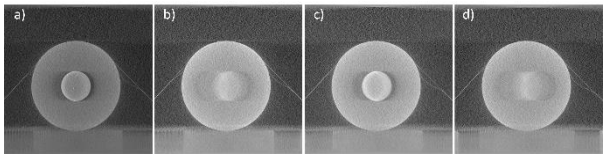

Fig. 4. Result from angular range 120°. (a) z_0, (b) $z=-1.7\text{mm}$, (c) $z=1.7\text{mm}$ (d) $z=3.4\text{mm}$ from z_0.

4. FURTHER STUDY

The final goal of this study is the application of these methods to the pCT for the PCB inspection. In order to accomplish it, further study is needed. First of all, it should be verified by experiment that the algorithm works correctly. Once we prove the algorithm is correct for the PCB phantom, then the results of reconstruction images will be compared by using metric parameters.

ACKNOWLEDGEMENT

This work was supported by the National Research Foundation of Korea (NRF) grant funded by the Korea government (MSIP) (No. 2013M2A2A9046313).

REFERENCES

[1] L. A. Feldkamp, L. C. Davis, and J. W. Kress, Practical cone-beam algorithm, *J. Opt. Soc. Am. A.*, Vol. 1, pp. 612-619, 1984.
[2] A. C. Kak and M. Slaney, Principles of computerized tomographic imaging, IEEE press, New York, 1988.
[3] G. Lauritsch and W. H. Härer, Theoretical framework for filtered back projection in tomosynthesis, *Proc. SPIE*, Vol. 3338, pp. 1127–1137, 1998.
[4] T. Wu, R. H. Moore, E. A. Rafferty, and D. B. Kopans, A comparison of reconstruction algorithms for breast tomosynthesis, *Med. phys.*, Vol. 31, pp. 2636–2647, 2004.
[5] H. Youn, J. S. Kim, M. K. Cho, S. Y. Jang, W. Y. Song, and H. K. Kim, Optimizing imaging conditions in digital tomosynthesis for image-guided radiation therapy, *Korean J. Med. Phys.*, Vol. 21, pp. 281-290, 2010.